

# Design Principles for a Single-Process 3D-Printed Accelerometer - Theory and Experiment

Matic Arh, Janko Slavič, Miha Boltežar

<sup>a</sup>*University of Ljubljana, Faculty of Mechanical Engineering, Aškerčeva 6, 1000 Ljubljana, Slovenia*

## *Cite as:*

*Matic Arh, Janko Slavič, and Miha Boltežar, Design principles for a single-process 3d-printed accelerometer – theory and experiment, Mechanical Systems and Signal Processing, Volume 152, May 2021, <https://doi.org/10.1016/j.ymsp.2020.107475>*

---

## **Abstract**

Fused-filament fabrication, one of the most accessible additive manufacturing technology, has already been used to manufacture piezoresistive static/quasistatic strain sensors, force sensors and wind sensors. Recent research showed that fused-filament fabrication could also be used for the manufacturing of dynamic sensors. However, the anisotropic mechanical and piezoresistive behaviour, the heterogeneity, the large number of process parameters and the large number of possible geometrical designs open up numerous design options for manufacturing. Additionally, a small size is difficult to achieve due to the relatively low geometrical tolerances and the resolution of fused-filament fabrication. This paper is focused on the design principles of a single-process, fused-filament fabricated, uni-axial accelerometer with a piezoresistive sensing element. The anisotropic piezoresistive behaviour is researched for the maximum sensitivity in the measured acceleration direction and the minimal cross-axis sensitivity for the perpendicular axes. The analytical accelerometer model is based on a Bernoulli-Euler beam and is used to understand the frequency and the geometrical influences of the piezoresistive accelerometer with a beam-shaped sensing element and an attached inertial mass. Finally, a small-sized ( $22 \times 22 \times 15 \text{ mm}^3$ ), single-axis, prototype accelerometer, with an approximately linear response up to 425 Hz and a low cross-axis sensitivity was manufactured. The derived principles can be used for further optimisation of the developed prototype sensor and

---

*Email address:* [janko.slavic@fs.uni-lj.si](mailto:janko.slavic@fs.uni-lj.si) (Janko Slavič)

as a foundation for the derivation of design principles for other types of fused-filament fabricated accelerometers, including 3-axis accelerometers.

*Keywords:* accelerometer, piezoresistivity, additive manufacturing, fused filament fabrication, dynamic sensor, 3D printing

---

## 1. Introduction

Recent advances in additive manufacturing (AM) have enabled the creation of end-products [1] and even smart structures *e.g.*, metamaterials [2, 3], energy harvesters [4], actuators [5, 6] and sensors [7, 8].

AM technologies can be used to create an accelerometer; however, seven different AM technology principles [9] and different sensing possibilities (piezoresistivity, capacitance, piezoelectricity, *etc.*) open up numerous design options. In the earliest studies, AM was used to manufacture the housing, while inserting conventionally manufactured accelerometers as the sensing element [10]. In 2018 and 2019, combining stereolithography (SLA) and wet-metallization, Zega *et al.* manufactured single axis [11] and three-axis [12] capacitive accelerometers, respectively. In 2020 Liu *et al.* [13], developed a fully printed piezoresistive accelerometer using SLA, screen-printing technology and direct ink writing.

Another promising AM technology for manufacturing accelerometers is fused-filament fabrication (FFF) as it enables the simultaneous printing of insulating and stimuli-sensitive materials. This allows the single-process manufacturing of the accelerometer's housing and the sensing element. An additional advantage is the low cost of a FFF machines and therefore the wide applicability.

When using FFF, piezoresistivity can be used as the sensing principle. Piezoresistivity denotes the strain dependent electrical resistivity [14]. In order to exhibit piezoresistivity, a material has to be electrically conductive; however, thermoplastic materials are used for FFF and they are electrically non-conductive. But by including conductive particles in the non-conductive polymer matrix, electrical conductivity can be achieved [15]. The volume ratio between the conductive particles and the non-conductive matrix has to exceed the percolation threshold, in order to conduct an electrical current [16]. Several conductive composites can be used for FFF, such as acrylonitrile butadiene styrene (ABS)/carbon nanotubes (CNT) [17], ABS/multiwalled carbon nanotubes (MWCNT) [18], nylon 6/metal and high-density polyethylene [19], polypropylene/carbon black [20], thermoplastic polyurethane (TPU)/MWCNT [21, 22] and polylactic acid (PLA)/carbon

black [23]. In addition to the type and amount of conductive particles, the FFF process parameters significantly impact on the achieved conductivity/resistivity of FFF structures [24]. The resistivity of the fabricated parts is temperature dependent as well [25].

In 2012 Leigh *et al.* [26] developed an electrically conductive material called “carbomorph” that was used with FFF technology. The applicability of the developed material with FFF for sensing applications was demonstrated on a 3D-printed glove able to sense finger movements. Afterwards, several static/quasi-static sensors were developed, including a graphene-based PLA and TPU composite sensor by Alsharari *et al.* [27], a TPU/MWCNT composite based sensor and bidirectional stretchable sensor by Christ *et al.* [21, 28], a flex sensors in soft pneumatic components by Hohimer *et al.* [29], load cell by Stano *et al.* [30], an embedded strain sensor by Gooding and Fields [31], a multiaxial force sensor by Kim *et al.* [32] and a wind sensor by Al-Rubaiai *et al.* [33]. The piezoresistive sensor’s behaviour is significantly influenced by the FFF process parameters; therefore, knowledge about piezoresistivity as a material- and process-dependent property is of great importance.

Most of piezoresistivity research was limited to resistance-change observations when a static [31, 34] and a cyclic [35] tensile load or a cyclic bending load [36] was applied. Only recently, a resistivity-strain tensor-based experimental method for dynamic piezoresistivity identification was introduced [37]. It was shown that a one-order-of-magnitude higher piezoresistive coefficient is obtained when the stress and electric field act perpendicular to the material deposition direction instead of parallel to it.

Recently, the piezoresistive-based dynamic<sup>1</sup> strain sensing of FFF structures was researched by Maurizi *et al.* [38, 39] and showed that FFF can be used in the future as a dynamic-sensors manufacturing technology. There are a large variety of accelerometer-design options due to the anisotropic mechanical and piezoresistive behaviour, the heterogeneity, the large number of process parameters with great influence on the mechanical and piezoresistive behaviour and the large number of possible geometrical designs. Numerous design options make it difficult and time-consuming to find optimal accelerometer. In order to reduce the accelerometer’s development time, it is important to neglect poor-performance accelerometer designs in the concept-development phase. A shorter time can be achieved by deriving and following the design principles for an FFF accelerometer.

---

<sup>1</sup>harmonic mechanical load in 5-4000 Hz frequency range

In the manuscript an analytical model based on the Bernoulli-Euler (BE) beam theory and a tensor-based, linear, piezoresistive material model is used to find the design principles for an FFF accelerometer. Based on the derived design principles, a showcase accelerometer is manufactured and experimentally researched. The manuscript is organized as follows: Sec. 2 gives the theoretical background to piezoresistive acceleration sensing, in Sec. 3 the design principles for an FFF accelerometer are derived, in Sec. 4 a showcase accelerometer is conceptualised, Sec. 5 gives the background to the accelerometer manufacturing procedure and experimental research, Sec. 6 presents the experimental results and Sec. 7 draws the conclusions.

## 2. Theoretical backgrounds

In a FFF piezoresistive accelerometer, the base acceleration  $\ddot{w}_b$  induces, due to the inertial effects, the mechanical strain  $\epsilon$ , which results in a change of the electrical resistance  $dR$ :

$$\text{acceleration } \ddot{w}_b \longrightarrow \text{strain } \epsilon \longrightarrow \text{resistance change } dR.$$

Resistance change can be used as an acceleration indicator when the change is proportional to the applied acceleration [40].

The principle of operation for a piezoresistive accelerometer is presented in Fig. 1. The accelerometer consists of insulating and piezoresistive materials. Two electrodes are applied to the piezoresistive sensing element. Between the electrodes a constant resistance  $R = R_0$  exists in the case of no acceleration; however, when an acceleration is applied, both the insulating and piezoresistive parts deform and the resistance changes  $dR(\epsilon)$ , due to the applied strain  $\epsilon$ .

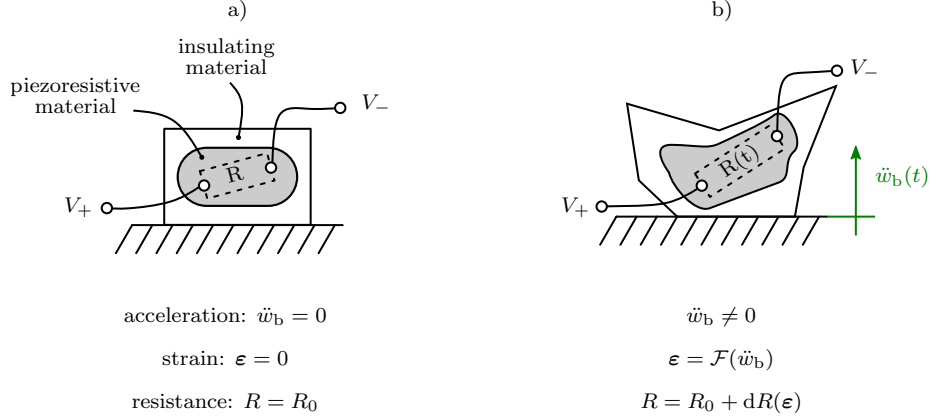


Figure 1: Piezoresistive accelerometer a) no base acceleration, b) base acceleration  $\ddot{w}_b$

The strain  $\epsilon$  in the FFF accelerometer depends on the applied acceleration  $\ddot{w}_b(t)$ , the geometrical design (shear-based, bending-based, tension-based), the bulk material properties and the FFF process parameters.

The resistance  $R$ , on the other hand, is the quotient between the voltage drop  $u$  and the current  $i$  [41]:

$$R = \frac{u}{i} = \frac{V_+ - V_-}{i}. \quad (1)$$

where  $u$  is defined by the applied voltages  $V_+$ ,  $V_-$ , see Fig. 1. The resistance can be written in terms of the electric field intensity  $\mathbf{E}$  and the electric current density  $\mathbf{J}$  [41]:

$$R = \frac{u}{i} = \frac{\int \mathbf{E} \cdot d\mathbf{l}}{\int_{\mathcal{A}(t)} \mathbf{J} \cdot d\mathbf{a}}, \quad (2)$$

where  $\mathcal{L}(t)$  denotes the integration path,  $\mathcal{A}(t)$  is the resistor's cross-section along the integration path and  $t$  is the time. Both the integration path  $\mathcal{L}(t)$  and the resistor's cross-section  $\mathcal{A}(t)$  can change over time due to the applied strain (due to the acceleration). The electric field intensity  $\mathbf{E}$  and the electric current density  $\mathbf{J}$  are, for homogeneous structures, related by Ohm's law in terms of the summation convention as [42]:

$$E_i = \rho_{ij} J_j, \quad i, j = 1, \dots, 3 \quad (3)$$

where  $i, j$  denote the coordinate system components and  $\rho_{ij}$  the resistivity component relating the electric field intensity in the  $i$ -th direction and the electric current density in the  $j$ -th direction. The resistivity  $\rho_{ij}$  is the sum of the initial resistivity (when no strain is applied)  $\rho_{0ij}$  and the change of the resistivity due to the applied strain  $d\rho_{ij}$ :

$$\rho_{ij} = \rho_{0ij} + d\rho_{ij} = \rho_{0ij} \left( 1 + \frac{d\rho_{ij}}{\rho_{0ij}} \right). \quad i, j = 1, \dots, 3 \quad (4)$$

The relative resistivity change  $d\rho_{ij}/\rho_{0ij}$  depends on the strain [43]:

$$\frac{d\rho_{ij}}{\rho_{0ij}} = \xi_{ijkl} \varepsilon_{kl}, \quad i, j, k, l = 1, \dots, 3 \quad (5)$$

where  $\xi_{ijkl}$  denotes the piezoresistive coefficient and  $\varepsilon_{kl}$  the strain component. Using Voigt-Kelvin notation, which replaces the two-subscript notation by a single-subscript notation [44],

$$11 \rightarrow 1, \quad 22 \rightarrow 2, \quad 33 \rightarrow 3, \quad 23 \rightarrow 4, \quad 13 \rightarrow 5, \quad 12 \rightarrow 6 \quad (6)$$

Eq. (5) simplifies to

$$d\rho_i/\rho_{0i} = \xi_{ij} \varepsilon_j, \quad i, j = 1, \dots, 6. \quad (7)$$

For structures with unidirectionally deposited material, orthotropy can be assumed [45]. The orthotropic resistivity and the matrix of piezoresistive coefficients from Eqs. (3) and (7), respectively, in the material coordinate system for a planar structure are:

$$\boldsymbol{\rho} = \begin{bmatrix} \rho_{11} & 0 \\ 0 & \rho_{22} \end{bmatrix}, \quad \boldsymbol{\xi} = \begin{bmatrix} \xi_{11} & \xi_{12} & 0 \\ \xi_{21} & \xi_{22} & 0 \\ 0 & 0 & \xi_{66} \end{bmatrix}. \quad (8)$$

The resistance  $R$  (2) can be written in terms of the electric current density (3):

$$R = \frac{\int_{\mathcal{L}(t)} \boldsymbol{\rho}(\boldsymbol{\varepsilon}) \cdot \mathbf{J} \cdot d\mathbf{l}}{\int_{\mathcal{A}(t)} \mathbf{J} \cdot d\mathbf{a}}, \quad (9)$$

Like with the resistivity  $\rho$  (4), the resistance  $R$  can be divided into the initial

resistance  $R_0$  and the resistance increment due to the applied strain  $dR$ :

$$R = R_0 + dR = R_0 \left( 1 + \frac{dR}{R_0} \right). \quad (10)$$

Eq. (9) indicates that the resistance  $R$  is the result of the geometrical properties and the resistivity  $\rho$ , which further depends on the exhibited strain field  $\varepsilon$ , the bulk material properties of the piezoresistive material, and the FFF process parameters.

### 3. Accelerometer design principles

In an accelerometer with an inertial mass, the acceleration  $\ddot{w}_b$  causes a change in the strain in the mass support structure  $\varepsilon$ , which further changes the relative resistance change  $dR(t)/R_0$ :

$$\ddot{w}_b(t) \quad \longrightarrow \quad \varepsilon(t) = \mathcal{F}(\ddot{w}_b) \quad \longrightarrow \quad \frac{dR(t)}{R_0} = \mathcal{G}(\varepsilon), \quad (11)$$

where the strain as a function of acceleration is  $\varepsilon = \mathcal{F}(\ddot{w}_b)$  and the relative resistance change as a function of strain is  $dR(t)/R_0 = \mathcal{G}(\varepsilon)$ . The accelerometer design principles are derived by observing the analytical expression of the relative resistance change as a function of the acceleration  $dR(t)/R_0 = \mathcal{H}(\ddot{w}_b)$ :

$$\frac{dR}{R_0} = \mathcal{H}(\ddot{w}_b) = \mathcal{G}(\mathcal{F}(\ddot{w}_b)) \quad (12)$$

The concept of the accelerometer, used to derive the analytical expression  $\mathcal{H}(\ddot{w}_b)$ , is presented in Fig. 2. The accelerometer consists of an inertial mass connected with the beam to the housing. In Fig. 2 a single beam is used; however, symmetrically arranged beams around the  $e_3$  axis will be used in the later experimental showcase. The sensing element consists of a non-piezoresistive material and a piezoresistive material with the resistivities  $\rho_c$  and  $\rho_p$  in the  $e_1$  direction, respectively. Voltages  $V_+$ ,  $V_-$  are applied to the conductive part of the housing, where no bending is exhibited. Dimensions  $l$ ,  $l_h$ , and  $\chi$  denote the length of the oscillating part of the beam, the length of the conductive track in the housing and the length of the piezoresistive element. The accelerations  $\ddot{w}_b(t)$  and  $\ddot{w}_{\text{rel}}(x, t)$  denote the base acceleration and the acceleration due to bending, respectively.

In the manuscript, Newton's dot notation (*e.g.*:  $\ddot{\mathcal{I}}(x, t) = \partial^2 \mathcal{I} / \partial t^2$ ) is used for the time derivatives and Lagrange's notation for the positional

derivatives (e.g.,:  $\mathcal{I}''(x, t) = \partial^2 \mathcal{I} / \partial x^2$ ).

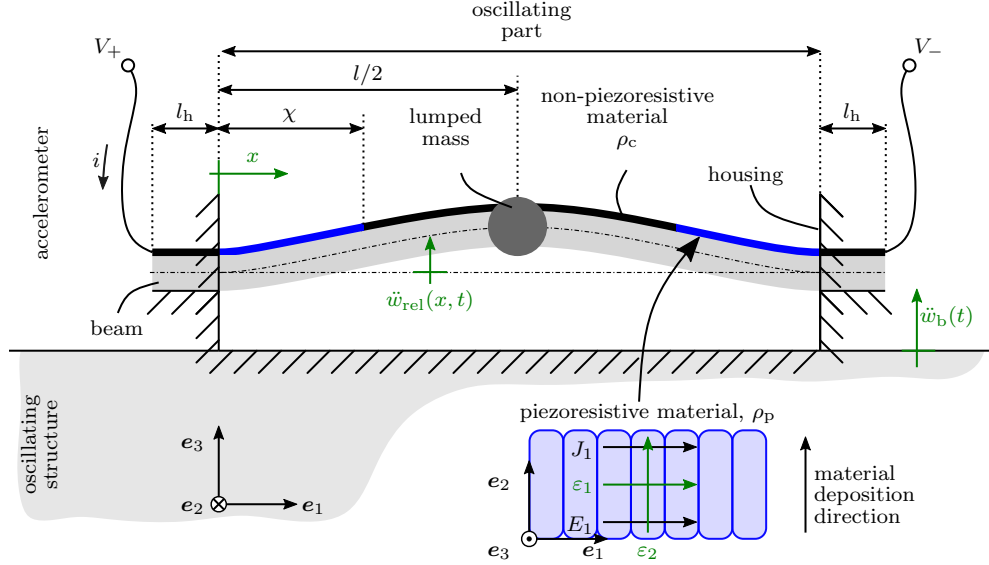


Figure 2: Accelerometer design

### 3.1. Strain as a function of acceleration

The Bernoulli-Euler (BE) beam theory is used to derive the exhibited strain  $\varepsilon = \mathcal{F}(\ddot{w}_b)$  in terms of the base excitation  $\ddot{w}_b$ . Transverse isotropy with isotropic properties in the horizontal plane of the insulating material is assumed [46, 47]. The physical model of the examined beam is shown in Fig. 3, with symmetry being taken into account. The strain in the beam  $\varepsilon_1$  in the direction  $e_1$  is defined as [48]:

$$\varepsilon_1 = -z w''(x, t), \quad (13)$$

where  $z$  is the coordinate of a certain point of the beam in the  $e_3$  direction with regard to the beam's centerline [48] and  $w(x, t)$  is the total displacement of the beam. The total displacement  $w(x, t)$  is the sum of the base displacement  $w_b(t)$  and the relative displacement due to bending  $w_{\text{rel}}(x, t)$ :

$$w(x, t) = w_b(t) + w_{\text{rel}}(x, t). \quad (14)$$

Since only the relative beam displacement  $w_{\text{rel}}(x, t)$  depends on the position  $x$ , the equation of motion (EOM) for a free vibrating BE beam, as

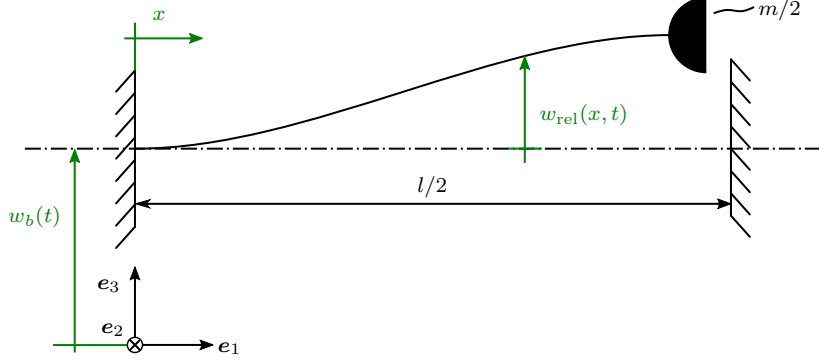


Figure 3: Physical model of the accelerometer

suming no damping, can be reformulated as [48]:

$$c^2 w_{\text{rel}}^{\text{IV}} + \ddot{w}_{\text{rel}} = -\ddot{w}_{\text{b}}. \quad (15)$$

with

$$c = \sqrt{\frac{Y I}{D A}}, \quad (16)$$

where  $Y$ ,  $I$ ,  $D$  and  $A$  denote Young's modulus, the second moment of the area about  $e_2$ , the density and the cross section of the beam, respectively.

Assuming that a harmonic base displacement is applied (17), then the relative displacement is harmonic as well (18):

$$w_{\text{b}}(t) = W_{\text{b}} e^{i\Omega t}, \quad (17)$$

$$w_{\text{rel}}(x, t) = W_{\text{rel}}(x) e^{i\Omega t}, \quad (18)$$

where  $W_{\text{b}}$  and  $W_{\text{rel}}(x)$  are the base displacement and the relative displacement amplitudes, respectively.  $\Omega$  is the angular excitation frequency,  $i$  is an imaginary unit and  $e$  is Euler's number. Inserting Eqs. (17), (18) into (15), yields:

$$W_{\text{rel}}^{\text{IV}}(x) - \beta^4 W_{\text{rel}}(x) = \beta^4 W_{\text{b}}. \quad (19)$$

with

$$\beta^4 = \frac{\Omega^2}{c^2} = \frac{D A \Omega^2}{Y I}. \quad (20)$$

Eq. (19) is of the same form as a forced beam with a constantly distributed transverse load [49]. The solution to Eq. (19) consists of a complementary part  $W_{\text{rel,c}}$  and a particular part  $W_{\text{rel,p}}$  [49]:

$$W_{\text{rel}}(x) = W_{\text{rel,c}}(x) + W_{\text{rel,p}}, \quad (21)$$

$$W_{\text{rel,p}} = -W_{\text{b}}, \quad (22)$$

$$W_{\text{rel,c}}(x) = K_0 \cos\left(\frac{b}{l}x\right) + K_1 \sin\left(\frac{b}{l}x\right) + \quad (23)$$

$$+ K_2 \cosh\left(\frac{b}{l}x\right) + K_3 \sinh\left(\frac{b}{l}x\right),$$

where  $b = \beta l$ . The constants  $K_0 - K_3$  are found from the following boundary conditions:

$$w_{\text{rel}}(0) = 0, \quad w'_{\text{rel}}(0) = 0, \quad w'_{\text{rel}}(l/2) = 0, \quad Y I w'''_{\text{rel}}(l/2) = \frac{m}{2} \ddot{w}(l/2), \quad (24)$$

After obtaining the coefficients  $K_0 - K_3$ , expressions for the beam's displacement  $w(x, t)$  and, consequently, the strain  $\varepsilon_1$  (13) are obtained; however, the trigonometric and hyperbolic terms in Eq. (24) are difficult to implement in any further derivation. Therefore, to simplify the analytical expression, a third-order Taylor expansion is used, as described in Appendix A. As discussed in the appendix, the simplified expression for the strain  $\varepsilon_1$  is valid when the ratio  $r_{\text{m}} = m/m_{\text{b}}$  between the inertial mass  $m$  and the mass of the beam  $m_{\text{b}}$  is greater than 1, and when the excitation frequency  $\Omega$  is significantly below the first natural frequency  $\omega_0$ . The simplified (linear with  $x$ ) expression is:

$$\varepsilon_1 = \mathcal{F}(\ddot{w}_{\text{b}}) \approx -z k \left( \frac{x}{l} - \frac{1}{4} \right) \ddot{W}_{\text{b}} e^{i\Omega t}, \quad (25)$$

with the proportionality constant  $k$  being:

$$k = \frac{96}{l^2 \omega_0^2}. \quad (26)$$

### 3.2. Relative resistance change as a function of strain

The relative resistance change  $dR/R_0$  corresponds to the sensor's sensitivity, see Eq.(10) and is defined as:

$$\frac{dR(t)}{R_0} = \frac{R(t) - R_0}{R_0}. \quad (27)$$

In order to obtain the relative resistance change  $dR(t)/R_0 = \mathcal{G}(\varepsilon)$  as a function of the strain  $\varepsilon$ , the resistance  $R(t)$  has to be written in terms of the strain, see Eq. (27). It is assumed that the piezoresistive material is unidirectionally deposited and therefore orthotropic [37]. Assuming a negligible contribution of the geometrical changes to the resistance change ( $\mathcal{A}$ ,  $\mathcal{L}$  are constant (9)), the resistance can be written as, see Eqs. (2), (9) and Fig. 2:

$$R(t) = \frac{2}{A_c} \int_{-l_h}^{l/2} \rho(x, t) dx, \quad (28)$$

where  $A_c$  denotes the cross-section of the sensing element and  $\rho(x, t)$  the resistivity along  $x$ , see Fig. 2:

$$\rho(x, t) = \begin{cases} \rho_c, & \text{if } -l_h < x \leq 0 \\ \rho_p(x, t), & \text{if } 0 < x \leq \chi \\ \rho_c, & \text{if } \chi < x \leq l/2 \end{cases}, \quad (29)$$

where  $\rho_c$  denotes the resistivity of the non-piezoresistive material, which does not depend on the strain and therefore the time and  $\rho_p(x, t)$  resistivity of the piezoresistive material, which is due to the piezoresistive nature, time and strain dependent and equal to:

$$\rho_p(x, t) = \rho_{0p} \left( 1 + \xi \varepsilon_1(x, t) \right), \quad (30)$$

where  $\rho_{0p}$  denotes the initial resistivity of the piezoresistive material and the piezoresistive coefficient  $\xi$  is due to Poisson's effect  $\varepsilon_2 = -\nu_{12} \varepsilon_1$ , the relationship in Eq. (8) and the Ohmic properties presented in Fig. 2:

$$\xi = \xi_{11} - \nu_{12} \xi_{12}. \quad (31)$$

The resistance at time  $t$  in terms of strain is, (28) (29), (30):

$$R(x, t) = \frac{2}{A_c} \left[ \rho_c (l_h + l/2 - \chi) + \rho_{0p} \chi + \rho_{0p} \xi \int_0^\chi \varepsilon_1(x, t) dx \right] \quad (32)$$

The initial resistance  $R_0$  represents the resistance of the accelerometer when no strain is exhibited and is equal to the resistance in Eq. (32) with the integral term being zero. The relative resistance change in terms of the

strain  $\mathcal{G}(\varepsilon)$  is therefore, see (27), (32):

$$\frac{dR}{R_0} = \mathcal{G}(\varepsilon) = \frac{\xi \int_0^\chi \varepsilon_1(x, t) dx}{\chi + \frac{\rho_c}{\rho_0 p} \left( l_h + \frac{l}{2} - \chi \right)}. \quad (33)$$

### 3.3. Relative resistance change as a function of the base acceleration

The relative resistance change  $dR/R_0 = \mathcal{H}(\ddot{w}_b)$  as a function of the base acceleration  $\ddot{w}_b$  is obtained by inserting Eq. (A.27) into Eq. (33):

$$\frac{dR}{R_0} = \mathcal{H}(\ddot{w}_b) = H_{\frac{dR}{R_0} \ddot{w}_b} \ddot{W}_b e^{i\Omega t}, \quad (34)$$

where  $H_{\frac{dR}{R_0} \ddot{w}_b}$  represents the frequency response function (FRF) [50, 51] between the relative resistance change and the base acceleration:

$$H_{\frac{dR}{R_0} \ddot{w}_b} = -\frac{\frac{\chi^2}{2} - \frac{l}{4} \chi}{\chi + \frac{\rho_c}{\rho_0 p} \left( l_h + \frac{l}{2} - \chi \right)} \xi z k. \quad (35)$$

FRF  $H_{\frac{dR}{R_0} \ddot{w}_b}$  corresponds to the sensor's sensitivity.

## 4. Showcase Design of a 3D-Printed Accelerometer

Here, the design principles of Sec. 3 will be applied to an experimental showcase. The operational frequency of the showcase should be up to 400 Hz, the cross-axis sensitivity should be small, the physical dimensions will be limited to  $25 \times 25 \times 10 \text{ mm}^3$ .

### 4.1. Mechanical design

Fig. 4 shows the researched support structure of the accelerometer design, where four beams (two at the top and two at the bottom) with an inertial mass in the middle are used to achieve translational motion (in  $\mathbf{e}_3$  direction) of the inertial mass, see also Fig. 2. The dimensions of a showcase accelerometer are shown in Fig. 4, using a finite element analysis with the isotropic material parameters<sup>2</sup>  $Y = 3.2 \text{ GPa}$ ,  $D = 1250 \text{ kg/m}^3$ , the first natural frequency is a translational mode in the  $\mathbf{e}_3$  direction at  $f_0 = 1425 \text{ Hz}$ .

---

<sup>2</sup>Isotropic properties are a reasonable approximation if 100% infill is used for the FFF printing and a linear region is examined [52]

As the first natural frequency is significantly above the expected frequency range of operation, it is expected that the higher modes will not have a significant influence in the directions  $e_1$ ,  $e_2$ .

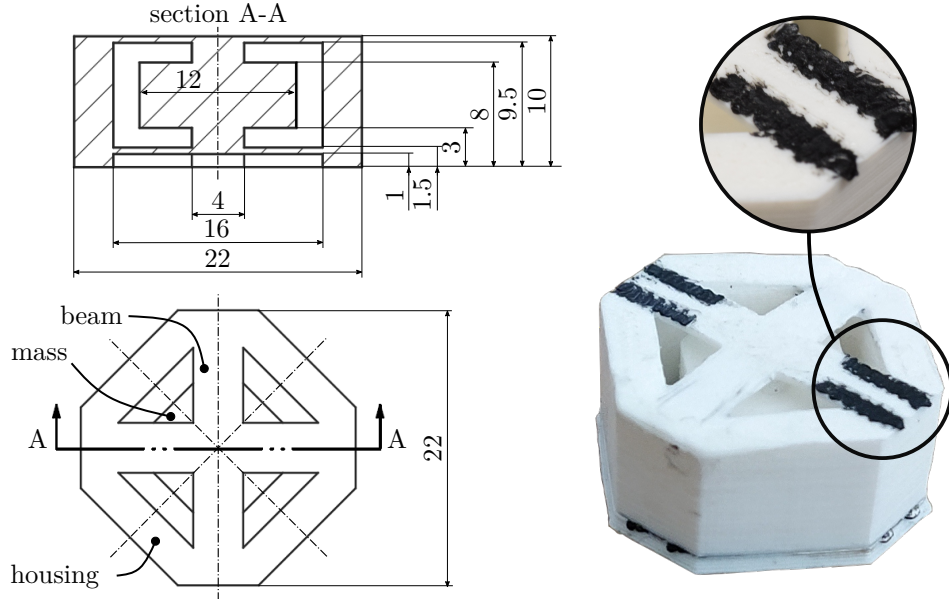


Figure 4: Dimension of a showcase accelerometer

#### 4.2. The design of the sensory element

Here, the sensory element is added to the supporting structure of the accelerometer. Based on Eq. (35) the sensing element will be defined for the highest sensitivity: the conductive track has been placed at the top or bottom of the beam (high  $z$  value), the piezoresistive coefficient  $\xi$  is increased by depositing piezoresistive material perpendicular to the applied strain  $\varepsilon_1$  and the electrical field  $E_1$  [37], see Figs. 2 and 4. Eq. (35) is further investigated for the length of the piezoresistive part  $\chi$ , for different resistivity ratios  $\rho_c/\rho_{0p}$  and the length of  $l_h$ , see 5. Fig. 5 reveals that a less than  $10^{-2}$  resistivity ratio  $\rho_c/\rho_{0p}$  is desired. To additionally increase the sensitivity, the length  $l_h$  (see Fig. 2) and the length of the piezoresistive part  $\chi$  should be minimised; in the showcase design accelerometer  $l_h \approx \chi \approx 0.2l$  was used. The mechanical design of the accelerometer also determines the coefficient  $k$  (26).

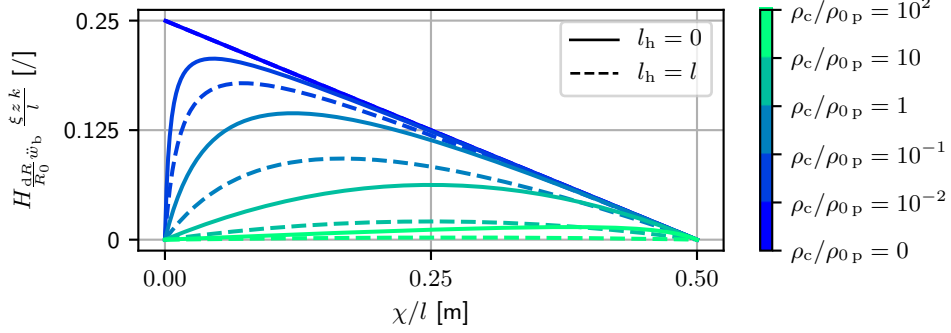


Figure 5: FRF  $H_{\frac{dR}{R_0} \dot{w}_b} \frac{\xi z k}{l}$  vs. relative length of piezoresistive element  $\chi/l$  for different resistivity ratios  $\rho_c/\rho_{0P}$  and length  $l_h$ .

#### 4.3. Electrical circuit

To increase the accelerometer's sensitivity while decreasing the cross-axis sensitivity, a full Wheatstone bridge is used. Instead of a single sensing track, four parallel tracks with resistances  $R_{S1} = 10.54 \text{ k}\Omega$ ,  $R_{S2} = 9.64 \text{ k}\Omega$ ,  $R_{S3} = 13.21 \text{ k}\Omega$  and  $R_{S4} = 14.74 \text{ k}\Omega$  are used, as shown in Fig. 6. The sensory elements  $R_{S1}$ ,  $R_{S3}$ , are placed at the top layer of the top beam and the sensory elements  $R_{S2}$ ,  $R_{S4}$ , at the bottom layer of the bottom beam. These elements are connected in a Wheatstone bridge, as shown in Fig. 6, whereby potentiometers  $R_{P1}$ ,  $R_{P2}$ ,  $R_{P3}$  and  $R_{P4}$  are connected in series with the sensory elements to balance the bridge ( $R_1 = R_2 = R_3 = R_4 = 16 \text{ k}\Omega$ , where  $R_i = R_{S_i+P_i}$ ). For a balanced bridge the voltage drop  $u_m$  is zero [53]; however, the strain causes a resistance change of the sensory elements  $dR_{S1}$ ,  $dR_{S2}$ ,  $dR_{S3}$  and  $dR_{S4}$ , causing a voltage change  $du_m$  as:

$$du_m = \frac{u}{4} \left( \frac{dR_1}{R_1} - \frac{dR_2}{R_2} + \frac{dR_3}{R_3} - \frac{dR_4}{R_4} \right), \quad (36)$$

where  $u = 12 \text{ V}$  denotes the supply voltage. When the accelerometer is excited in the  $e_3$  direction it operates in the bending mode. As a result, when the sensory elements in the top beam  $R_{S1}$ ,  $R_{S3}$  experience tension (positive resistance increment), the sensory elements in the bottom beam  $R_{S2}$ ,  $R_{S4}$  experience pressure (negative resistance increment); due to the negative sign in Eq.(36) the sensitivity is doubled. When excited in the  $e_1$  and  $e_2$  directions, all the sensory elements experience a simultaneous increase/decrease and the resistance increments are canceled out.

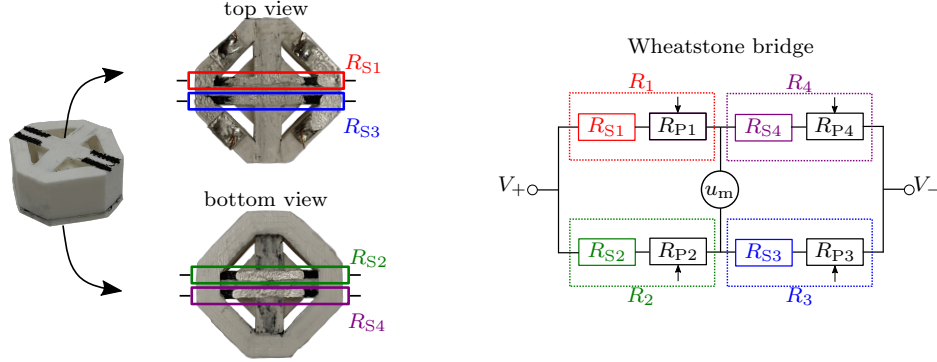


Figure 6: Eletrical circuit

## 5. Experiment

### 5.1. Manufacturing process

An Ultimaker 3 dual extrusion 3D printer was used to manufacture the accelerometer. A PLA filament from PLASTIKA TRČEK was used for the support structure and a PLA/carbon black Proto-pasta [23] for the sensory element. A polyvinyl alcohol (PVA) filament was used as the water-dissolvable support during printing. The PVA and conductive PLA filaments were printed through the same nozzle and were changed manually. The filaments diameter was 2.85 mm, the layer height 0.1 mm, the infill density 100 %, the built-plate temperature 60 °C and the line width 0.4 mm. A zig-zag infill pattern was used for the PLA and the lines pattern for the conductive PLA and PVA. Printing temperatures of 220 °C, 225 °C and 210 °C were used for the PLA, the conductive PLA and the PVA, respectively. The orientation of the lines was, for the conductive PLA, perpendicular to the beam directions (see Fig. 2). The 3D printed accelerometer was, for 2 days, sunk in warm water in order to dissolve the PVA printing support and then left for 1 day to dry. Afterwards the electrical contacts were prepared as described in Sec. 5.2.

### 5.2. Electrical contacts

In step 1, eight parallel piezoresistive tracks are 3D printed: 4 in the top layer of the top beam (Fig. 7 STEP 1) and 4 in the bottom layer of the bottom beam. In step 2, copper wire is soldered to a conductive tape [54], which is then taped to the supporting structure of the accelerometer (see Fig. 7 STEP 2). In step 3, silver conductive paint [55] is used to form purely

conductive paths between the copper wires and the sensory elements. The silver conductive paint represents the resistivity  $\rho_c = 10^{-6} \Omega \text{m}$  of length  $l_h = 3 \text{mm}$ .<sup>3</sup> In the future, steps 2 and 3 might become obsolete, as highly conductive printing material becomes viable [24].

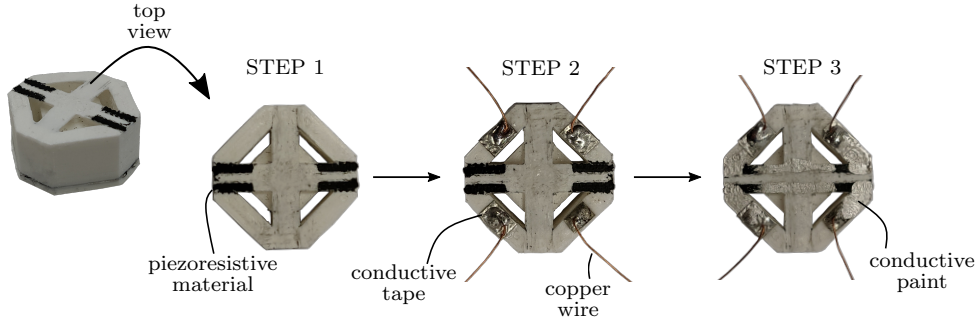


Figure 7: Preparation of electrical contacts, top view

### 5.3. Experimental setup

The sensitivity  $S_3$  and cross-axis sensitivities  $S_1$ ,  $S_2$  of the FFF accelerometer were measured. The sensitivity  $S_3$  was measured using an experimental setup shown in Fig. 8 a) and the cross-axis sensitivity  $S_1$  as it is shown in Fig. 8 b). The cross-axis sensitivity  $S_2$  was measured by rotating the accelerometer in Fig. 8 b) around the axis  $e_3$  for  $\pi/2$ . The FFF accelerometer was attached to the LDS V555 electrodynamical shaker. The base plate was excited with a sinusoidal acceleration with 1 g, 3 g and 5 g amplitudes at a constant frequency for 10 s. The excitation frequencies were in 25 Hz-1725 Hz range. The base acceleration  $\ddot{w}_b$  was measured using a PCB T333B30 accelerometer. The signals from the accelerometer and the FFF accelerometer were acquired using a National Instruments 9234 measuring card.

The measured voltage  $u_m$  and acceleration  $\ddot{w}_b$  were used to obtain the FRF  $H_{u_m \ddot{w}_b}(f)$ . The sensitivity and cross-axis sensitivities were obtained from the FRF  $H_{u_m \ddot{w}_b}(f_{\text{exc}})$  at the excitation frequency  $f_{\text{exc}}$ . For signal processing Python library SciPy [56] was used.

<sup>3</sup>Resistivity  $\rho_c$  is estimated under the assumption of a 0.1 mm thickness.

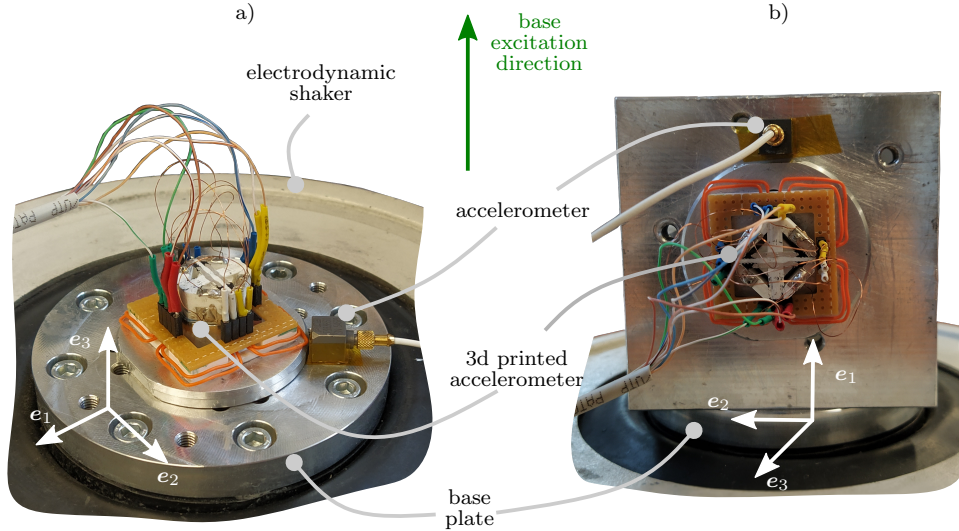


Figure 8: Experimental setup for measuring a) sensitivity  $S_3$  and b) cross-axis sensitivity  $S_1$  of FFF accelerometer

## 6. Results

In Fig. 9 the measured voltage amplitude spectrum  $|U_m(f)|$  and FRF  $H_{u_m \ddot{w}_b}$  for excitations in the  $e_1$ ,  $e_2$  and  $e_3$  directions at a 1 g, 3 g and 5 g base excitation amplitude  $\ddot{W}_b$  are presented. The FRF  $H_{u_m \ddot{w}_b}$  for the applied excitation in the  $e_3$  direction corresponds to the sensitivity  $S_3$  and in the  $e_1$ ,  $e_2$  directions corresponds to the cross-axis sensitivities  $S_1$ ,  $S_2$  respectively. Based on Fig. 9 and the results in Tab. 1 the following observations can be made: 1. the first natural frequency of the sensor is at approximately 1615 Hz, 2. the voltage amplitude spectrum  $|U_m|$  for measurements when acceleration is applied in the  $e_3$  direction is more than one order of magnitude above the noise-floor range, 3. the voltage amplitude spectrum  $|U_m|$  for measurements when the acceleration is applied in the  $e_1$  and  $e_2$  directions is the same order of magnitude as the noise-floor range, 4. the sensitivity  $13.01 - 14.19 \mu\text{V s}^2/\text{m}$  was measured in the 25-425 Hz range for the 1 g and 5 g excitation amplitudes, 6. the cross-axis sensitivity in  $e_1$  and  $e_2$  depends on the amplitude of the excitation and is, for most measurements, below 5%, (one measurement is at 8.5 %).

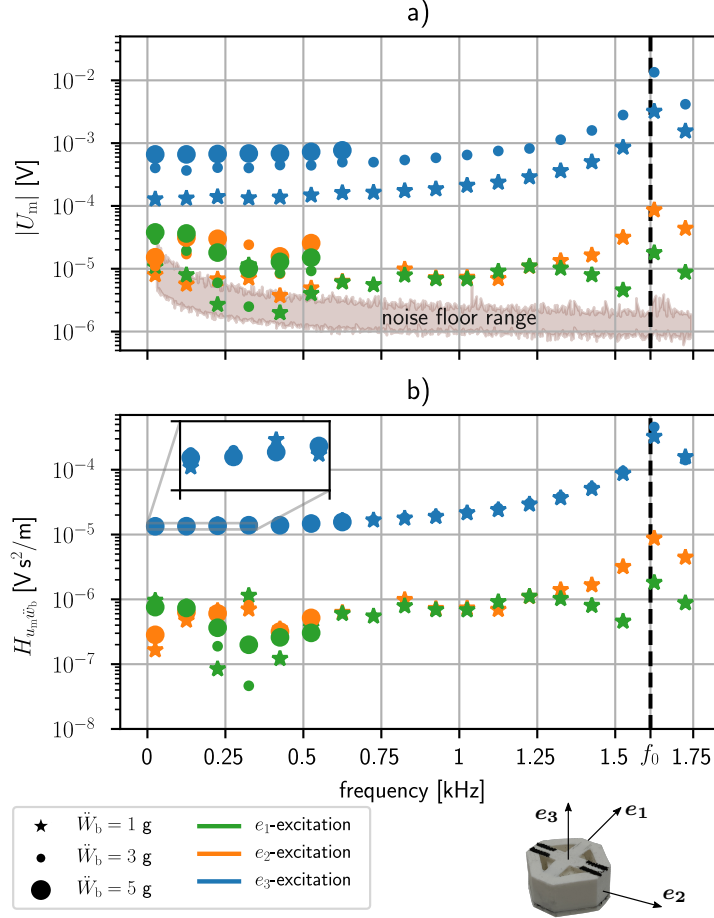


Figure 9: Measured a) voltage amplitude spectrum  $U_m$  and b) FRF  $H_{u_m \ddot{w}_b}$

## 7. Conclusions

The Bernoulli-Euler beam theory and the linear-resistivity-strain tensor-based piezoresistive material model were used to derive the design principles for FFF accelerometers with the strain and electric field established in the same direction.

The derived principles for the inertial, sub natural frequency, accelerometer are: 1. the highest possible piezoresistive coefficient  $\xi$  has to be achieved (finding the optimal material and process parameters), 2. piezoresistive tracks have to be perpendicular to the strain direction, 3. the sensing element has to be located at the bottom or top of the beam (highest possible

Table 1: Measured sensitivity  $S_3$  and cross-axis sensitivities  $S_1$ ,  $S_2$  in 25 Hz-525 Hz frequency range for 1 g and 5 g excitation amplitudes

$f$ [Hz]	$S_1$ [ $\mu\text{V s}^2/\text{m}$ ]		$S_2$ [ $\mu\text{V s}^2/\text{m}$ ]		$S_3$ [ $\mu\text{V s}^2/\text{m}$ ]		$S_1/S_3$ [%]		$S_2/S_3$ [%]	
	$\ddot{w}_b=1\text{ g}$	$\ddot{w}_b=5\text{ g}$	$\ddot{w}_b=1\text{ g}$	$\ddot{w}_b=5\text{ g}$	$\ddot{w}_b=1\text{ g}$	$\ddot{w}_b=5\text{ g}$	$\ddot{w}_b=1\text{ g}$	$\ddot{w}_b=5\text{ g}$	$\ddot{w}_b=1\text{ g}$	$\ddot{w}_b=5\text{ g}$
25	0.96	0.76	0.17	0.28	13.01	13.42	7.38	5.66	1.27	2.11
125	0.76	0.74	0.47	0.63	13.41	13.45	5.68	5.48	3.54	4.71
225	0.08	0.36	0.67	0.61	14.19	13.66	0.59	2.67	4.71	4.44
325	1.14	0.20	0.70	0.55	13.56	13.93	8.43	1.43	5.19	3.95
425	0.12	0.26	0.35	0.32	13.93	13.91	0.87	1.86	2.50	2.29
525	0.37	0.30	0.48	0.52	15.06	14.78	2.49	2.06	3.18	3.50

$z$  value), 4. the ratio between the initial resistivity of the conductive non-piezoresistive and piezoresistive material  $\rho_c/\rho_{0p}$  should be minimised, 5. the piezoresistive material should be located as close to the fixed housing of the accelerometer, while the length of the housing  $l_h$  should be minimised.

Based on the derived principles, a showcase FFF accelerometer with dimensions of  $22 \times 22 \times 15 \text{ mm}^3$  was manufactured. A Wheatstone bridge was used to improve the sensing performance. The first natural frequency of the accelerometer was at approximately 1615 Hz. An approximately linear response in the 25-425 Hz frequency range and 1-5 g acceleration amplitude was measured (less than 10 % difference, most measurements had 5 % or less of cross-axis sensitivity).

This research shows that FFF technology can be used to manufacture relatively small and reliable accelerometers. However, knowledge about the mechanical, resistive and piezoresistive behaviour is vital to achieve high sensitivity. It is expected that future research will further enhance the properties of the single-process 3D-printed accelerometers.

## Acknowledgements

The authors acknowledge the partial financial support from the Slovenian Research Agency (research core funding No. P2-0263).

## Appendix A. Simplification of Bernoulli-Euler beam

The total displacement of the base excited beam from Fig. 3 is defined as, see Sec. 3.1:

$$w(x, t) = w_b(t) + w_{\text{rel}}(x, t), \quad (\text{A.1})$$

$$w_b(t) = W_b e^{i\Omega t}, \quad (\text{A.2})$$

$$w_{\text{rel}}(x, t) = W_{\text{rel}}(x) e^{i\Omega t}, \quad (\text{A.3})$$

$$\begin{aligned} W_{\text{rel}}(x) = & K_0 \cos\left(\frac{b}{l} x\right) + K_1 \sin\left(\frac{b}{l} x\right) + \\ & + K_2 \cosh\left(\frac{b}{l} x\right) + K_3 \sinh\left(\frac{b}{l} x\right) - W_b. \end{aligned} \quad (\text{A.4})$$

The constants  $K_0 - K_3$  are found from the following boundary conditions:

$$w_{\text{rel}}(0) = 0, \quad w'_{\text{rel}}(0) = 0, \quad w'_{\text{rel}}(l/2) = 0, \quad Y I w'''_{\text{rel}}(l/2) = \frac{m}{2} \ddot{w}(l/2), \quad (\text{A.5})$$

which leads to the system of equations:

$$K_0 + K_2 = W_b, \quad (\text{A.6})$$

$$K_1 + K_3 = 0, \quad (\text{A.7})$$

$$K_0 \sin\left(\frac{b}{2}\right) - K_1 \cos\left(\frac{b}{2}\right) - K_2 \sinh\left(\frac{b}{2}\right) - K_3 \cosh\left(\frac{b}{2}\right) = 0, \quad (\text{A.8})$$

$$\begin{aligned} & K_0 \left[ r_m b \cos\left(\frac{b}{2}\right) + 2 \sin\left(\frac{b}{2}\right) \right] + K_1 \left[ r_m b \sin\left(\frac{b}{2}\right) - 2 \cos\left(\frac{b}{2}\right) \right] + \\ & + K_2 \left[ r_m b \cosh\left(\frac{b}{2}\right) - 2 \sinh\left(\frac{b}{2}\right) \right] + K_3 \left[ r_m b \sinh\left(\frac{b}{2}\right) - 2 \cosh\left(\frac{b}{2}\right) \right] = 0, \end{aligned} \quad (\text{A.9})$$

where  $r_m$  represents the mass ratio between the lumped mass  $m$  and the mass of the beam  $m_b$  and is:

$$r_m = \frac{m}{m_b} = \frac{m}{D A l}. \quad (\text{A.10})$$

The obtained coefficients are:

$$\begin{aligned} K_0 &= W_b - K_2 = & (A.11) \\ &= \frac{W_b}{2} \frac{b r_m \left[ \cos\left(\frac{b}{2}\right) \cosh\left(\frac{b}{2}\right) - 1 \right] + \sinh\left(\frac{b}{2}\right) \left[ 4 \cos\left(\frac{b}{2}\right) - b r_m \sin\left(\frac{b}{2}\right) \right]}{2 \cos\left(\frac{b}{2}\right) \sinh\left(\frac{b}{2}\right) - b r_m + \cosh\left(\frac{b}{2}\right) \left[ 2 \sin\left(\frac{b}{2}\right) + b r_m \cos\left(\frac{b}{2}\right) \right]}, \end{aligned}$$

$$\begin{aligned} K_1 &= -K_3 = & (A.12) \\ &= \frac{W_b}{2} \frac{b r_m \sin\left(\frac{b}{2}\right) \cosh\left(\frac{b}{2}\right) + \sinh\left(\frac{b}{2}\right) \left[ 4 \sin\left(\frac{b}{2}\right) + b r_m \cos\left(\frac{b}{2}\right) \right]}{2 \cos\left(\frac{b}{2}\right) \sinh\left(\frac{b}{2}\right) - b r_m + \cosh\left(\frac{b}{2}\right) \left[ 2 \sin\left(\frac{b}{2}\right) + b r_m \cos\left(\frac{b}{2}\right) \right]}. \end{aligned}$$

Eqs. (A.11), (A.12) show that  $W_b$  is expressible from the constants  $K_0$ - $K_3$  as:

$$K_0 = k_0(b, r_m) W_b, \quad (A.13)$$

$$K_1 = k_1(b, r_m) W_b, \quad (A.14)$$

$$K_2 = k_2(b, r_m) W_b, \quad (A.15)$$

$$K_3 = k_3(b, r_m) W_b. \quad (A.16)$$

Since the base displacement amplitude  $W_b$  is related to the acceleration amplitude  $\ddot{W}_b = -\Omega^2 W_b$ , the second position derivative  $w''$  in terms of the acceleration amplitude  $\ddot{W}_b$  can be derived, see Eqs. (14), (17), (18), (21)-(24), (A.11), (A.12), (A.13)-(A.16):

$$w'' = -\mathcal{W}(b, r_m, x) \frac{\ddot{W}_b}{\Omega^2} e^{i\Omega t}, \quad (A.17)$$

where  $\mathcal{W}(b, r_m, x)$  represents:

$$\mathcal{W} = \frac{b^2}{l^2} \left[ -k_0 \cos\left(\frac{b}{l} x\right) - k_1 \sin\left(\frac{b}{l} x\right) + k_2 \cosh\left(\frac{b}{l} x\right) + k_3 \sinh\left(\frac{b}{l} x\right) \right] \quad (A.18)$$

An accelerometer normally operates significantly below the first natural frequency  $\Omega < 0.5\omega_0$ , where  $\omega_0$  denotes the first natural frequency. If the parameter  $b_0$  denotes the parameter  $b$  at the natural frequency  $\omega_0$ :

$$b_0 = b(\Omega = \omega_0) = \sqrt[4]{\frac{D A \omega_0^2}{Y I}} l, \quad (A.19)$$

then  $b$  can be expressed in terms of  $b_0$  as:

$$b = r^{1/2} b_0(r_m), \quad (\text{A.20})$$

where the relative frequency  $r = \Omega/\omega_0$  represents the ratio between the excitation frequency  $\Omega$  and the first natural frequency  $\omega_0$ . Parameter  $b_0$  depends on the mass ratio  $r_m$  and is obtained from natural frequency equation of a beam clamped at both ends and the mass in the center [57]:

$$\frac{r_m b_0}{2} \left[ \cos\left(\frac{b_0}{2}\right) \cosh\left(\frac{b_0}{2}\right) - 1 \right] + \cos\left(\frac{b_0}{2}\right) \sinh\left(\frac{b_0}{2}\right) + \sin\left(\frac{b_0}{2}\right) \cosh\left(\frac{b_0}{2}\right) = 0 \quad (\text{A.21})$$

A closed form approximation can be used to estimate  $b_0$  as [57]:

$$b_{0 \text{ app}} \approx \frac{192}{r_m + \frac{13}{560}}. \quad (\text{A.22})$$

The solutions  $b_0$  of the transcendental equation (A.21) and the approximation  $b_{0 \text{ app}}$  (A.22) for different mass ratios  $r_m$  are shown in Tab. A.2. The approximation is close to the real value, when the ratio  $r_m$  increases, see Tab. A.2.

Table A.2: Solution to the Eq. (A.21) for different mass ratios  $r_m$  [57]

$r_m$	0	0.1	0.5	1	2	5	10	100
$b_0$	4.730	4.46	3.846	3.440	3.000	2.446	2.072	1.1760
$b_{0 \text{ app}}$	9.953	6.29	4.37	3.7	3.120	2.488	2.092	1.1772

Using relationship (A.20), the function  $\mathcal{W}$  can be written in terms of the relative frequency  $r$  and the parameter  $b_0$ . Since the accelerometer operates below the first natural frequency and since the maximum  $b_0$  value is 4.730, see Tab. A.2, a third-order Taylor expansion is used, to simplify the trigonometric and hyperbolic functions in Eq. (A.18):

$$\mathcal{W}_{\text{Tay}} = \frac{r^2 b_0^4}{2 l^2} \left( \frac{x^2}{l^2} - \frac{x}{l} \frac{3 \left( r^2 b_0^4 - 192 \right) r_m + r^2 b_0^4 - 576}{3 r^2 b_0^4 (r_m + 1) - 576} + \frac{\left( r^2 b_0^4 - 288 \right) r_m - 192}{6 r^2 b_0^4 (r_m + 1) - 1152} \right) \quad (\text{A.23})$$

where  $\mathcal{W}_{\text{Tay}}$  denotes the simplified function  $\mathcal{W}$ . In Fig. A.10 a), solid lines represent analytical function  $\mathcal{W} l^2$  vs. position  $x$  at  $r = 0.1$  relative frequency and different mass ratios  $r_m$ .  $\mathcal{W} l^2$  converges to a linear function, when  $r_m$  increases; therefore,  $\mathcal{W}_{\text{Tay}}$  is examined, when  $r_m$  converges to infinity. Due

to an “infinite”  $r_m$ , approximation  $b_{0\text{ app}}$  can be used and it follows:

$$\lim_{r_m \rightarrow \infty} \mathcal{W}_{\text{Tay}} = -\frac{24 r^2}{(r^2 - 1) l^2} + \frac{96 r^2}{(r^2 - 1) l^3} x \quad (\text{A.24})$$

Since the accelerometer operates significantly below the first natural frequency  $r \ll 1$ , the relative frequency in the denominator is neglected and Eq. (A.24) is simplified as:

$$\mathcal{W}_{\text{app}} = -\frac{96 r^2}{l^2} \left( \frac{x}{l} - \frac{1}{4} \right). \quad (\text{A.25})$$

The approximation  $\mathcal{W}_{\text{app}} l^2$  with regard to the position  $x$  at  $r = 0.1$  is presented in Fig. A.10 a). In Fig. A.10 b) an analytical function  $\mathcal{W} l^2$  for different mass ratios  $r_m$  and an approximation  $\mathcal{W}_{\text{app}} l^2$  vs. relative frequency  $r$  at position  $x = l/2$  is shown. Eq. (25) is inserted in Eqs. (A.17), (13) and the strain as a function of the acceleration is obtained  $\varepsilon_1 = \mathcal{F}(\ddot{w}_b)$ :

$$\varepsilon_1 = \mathcal{F}(\ddot{w}_b) \approx H_{\varepsilon_1 \ddot{w}_b} \ddot{W}_b e^{i\Omega t}, \quad (\text{A.26})$$

where  $H_{\varepsilon_1 \ddot{w}_b}$  represents the FRF between the strain  $\varepsilon_1$  and the acceleration  $\ddot{w}_b$ :

$$H_{\varepsilon_1 \ddot{w}_b} = -z \frac{96}{l^2 \omega_0^2} \left( \frac{x}{l} - \frac{1}{4} \right). \quad (\text{A.27})$$

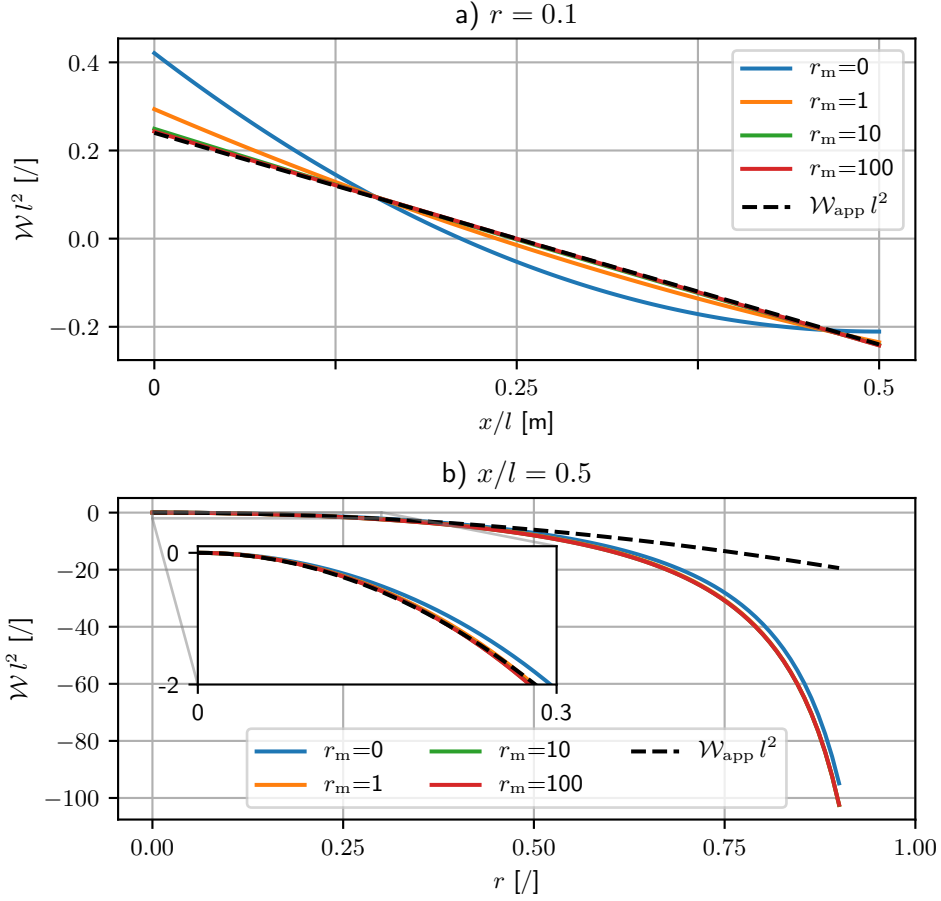


Figure A.10: Function  $\mathcal{W}l^2$  a) versus position  $x$  at relative frequency  $r = 0.1$  b) versus relative frequency  $r$  at position  $x = l/2$

## References

- [1] Tuan D Ngo, Alireza Kashani, Gabriele Imbalzano, Kate T Q Nguyen, and David Hui. Additive manufacturing (3D printing): A review of materials, methods, applications and challenges. *Composites Part B: Engineering*, 143:172–196, 2018.
- [2] Adriano T. Fabro, Han Meng, and Dimitrios Chronopoulos. Uncertainties in the attenuation performance of a multi-frequency metastructure from additive manufacturing. *Mechanical Systems and Signal Processing*, 138:106557, 2020.

- [3] C. Claeys, E. Deckers, B. Pluymers, and W. Desmet. A lightweight vibro-acoustic metamaterial demonstrator: Numerical and experimental investigation. *Mechanical Systems and Signal Processing*, 70-71:853–880, 2016.
- [4] Abdullah Nammari, Logan Caskey, Johnny Negrete, and Hamzeh Bardaweel. Fabrication and characterization of non-resonant magneto-mechanical low-frequency vibration energy harvester. *Mechanical Systems and Signal Processing*, 102:298–311, 2018.
- [5] Sampada Bodkhe, Lorenzo Vigo, Shengyun Zhu, Oleg Testoni, Nicole Aegerter, and Paolo Ermanni. 3D Printing To Integrate Actuators Into Composites. *Additive Manufacturing*, 35(May):101290, 2020.
- [6] Liang Wang, Viktor Hofmann, Fushi Bai, Jiamei Jin, and Jens Twiefel. A novel additive manufactured three-dimensional piezoelectric transducer: Systematic modeling and experimental validation. *Mechanical Systems and Signal Processing*, 114:346–365, 2019.
- [7] Jong-yun Yoon and Gi-woo Kim. Harnessing the bilinear nonlinearity of a 3D printed biomimetic diaphragm for acoustic sensor applications. *Mechanical Systems and Signal Processing*, 116:710–724, 2019.
- [8] Xingxu Zhang, Xiaobiao Shan, Tao Xie, and Jianmin Miao. A new sensor inspired by the lateral-line system of fish using the self-powered d33 mode piezoelectric diaphragm for hydrodynamic sensing. *Mechanical Systems and Signal Processing*, 141:106476, 2020.
- [9] ASTM 52900:2015. Standard Terminology for Additive Manufacturing – General Principles – Terminology. *ASTM International*, i:1–9, 2015.
- [10] Eric MacDonald, Rudy Salas, David Espalin, Mireya Perez, Efrain Aguilera, Dan Muse, and Ryan B. Wicker. 3D printing for the rapid prototyping of structural electronics. *IEEE Access*, 2:234–242, 2014.
- [11] Valentina Zega, Caterina Credi, Roberto Bernasconi, Giacomo Langfelder, Luca Magagnin, Marinella Levi, and Alberto Corigliano. The first 3-d-printed z-axis accelerometers with differential capacitive sensing. *IEEE Sensors Journal*, 18(1):53–60, 2018.
- [12] Valentina Zega, Marta Invernizzi, Roberto Bernasconi, Federico Cuneo, Giacomo Langfelder, Luca Magagnin, Marinella Levi, and Alberto

- Corigliano. The First 3D-Printed and Wet-Metallized Three-Axis Accelerometer with Differential Capacitive Sensing. *IEEE Sensors Journal*, 19(20):9131–9138, 2019.
- [13] Mingjie Liu, Qi Zhang, Yulong Zhao, Yiwei Shao, and Dongliang Zhang. Design and development of a fully printed accelerometer with a carbon paste-based strain gauge. *Sensors (Switzerland)*, 20(12):1–17, 2020.
- [14] G. M. Koo and T. N. Tallman. Higher-order resistivity-strain relations for self-sensing nanocomposites subject to general deformations. *Composites Part B: Engineering*, 190(December 2019):107907, 2020.
- [15] J.C. Tan and H.Y. Low. Multi-materials fused filament printing with embedded highly conductive suspended structures for compressive sensing. *Additive Manufacturing*, page 101551, August 2020.
- [16] A S Fiorillo, C D Critello, and S A Pullano. Theory, technology and applications of piezoresistive sensors: A review. *Sensors and Actuators A: Physical*, 281:156–175, 2018.
- [17] Sithiprumnea Dul, Luca Fambri, and Alessandro Pegoretti. Filaments Production and Fused Deposition Modelling of ABS/Carbon Nanotubes Composites. *Nanomaterials (Basel, Switzerland)*, 8(1), January 2018.
- [18] A Dorigato, V Moretti, S Dul, S H Unterberger, and A Pegoretti. Electrically conductive nanocomposites for fused deposition modelling. *Synthetic Metals*, 226:7–14, 2017.
- [19] J C Tan and H Y Low. Embedded electrical tracks in 3D printed objects by fused filament fabrication of highly conductive composites. *Additive Manufacturing*, 23:294–302, 2018.
- [20] Sen Wai Kwok, Kok Hin Henry Goh, Zer Dong Tan, Siew Ting Melissa Tan, Weng Weei Tjiu, Je Yeong Soh, Zheng Jie Glenn Ng, Yan Zhi Chan, Hui Kim Hui, and Kuan Eng Johnson Goh. Electrically conductive filament for 3D-printed circuits and sensors. *Applied Materials Today*, 9:167–175, 2017.
- [21] Josef F Christ, Nahal Aliheidari, Amir Ameli, and Petra Pötschke. 3D printed highly elastic strain sensors of multiwalled carbon nanotube/thermoplastic polyurethane nanocomposites. *Materials & Design*, 131:394–401, 2017.

- [22] Myoungsuk Kim, Jaebong Jung, Sungmook Jung, Young Hoon Moon, Dae-Hyeong Kim, and Ji Hoon Kim. Piezoresistive behaviour of additively manufactured multi-walled carbon nanotube/thermoplastic polyurethane nanocomposites. *Materials*, 12(16):2613, August 2019.
- [23] Technical data - proto-pasta conductive pla. <https://www.proto-pasta.com/products/conductive-pla>. Last accessed 21. September 2020.
- [24] Tibor Barši Palmić, Janko Slavič, and Miha Boltežar. Process parameters for FFF 3d-printed conductors for applications in sensors. *Sensors*, 20(16):4542, August 2020.
- [25] Gianni Stano, Attilio Di Nisio, Anna Maria Lanzolla, Mattia Ragolia, and Gianluca Percoco. Fused filament fabrication of commercial conductive filaments: experimental study on the process parameters aimed at the minimization, repeatability and thermal characterization of electrical resistance. *The International Journal of Advanced Manufacturing Technology*, 111(9-10):2971–2986, November 2020.
- [26] Simon J Leigh, Robert J Bradley, Christopher P Pursell, Duncan R Billson, and David A Hutchins. A Simple, Low-Cost Conductive Composite Material for 3D Printing of Electronic Sensors. *PLOS ONE*, 7(11):e49365, November 2012.
- [27] Meshari Alsharari, Baixin Chen, and Wenmiao Shu. 3d printing of highly stretchable and sensitive strain sensors using graphene based composites. *Proceedings*, 2(13):792, December 2018.
- [28] Josef Christ, Nahal Aliheidari, Petra Pötschke, and Amir Ameli. Bidirectional and stretchable piezoresistive sensors enabled by multi-material 3d printing of carbon nanotube/thermoplastic polyurethane nanocomposites. *Polymers*, 11(1):11, December 2018.
- [29] Cameron J. Hohimer, Gayaneh Petrossian, Amir Ameli, Changki Mo, and Petra Pötschke. 3d printed conductive thermoplastic polyurethane/carbon nanotube composites for capacitive and piezoresistive sensing in soft pneumatic actuators. *Additive Manufacturing*, 34:101281, 2020.
- [30] Gianni Stano, Attilio Di Nisio, Annamaria Lanzolla, and Gianluca Percoco. Additive manufacturing and characterization of a load cell with embedded strain gauges. *Precision Engineering*, 62:113 – 120, 2020.

- [31] Jesse Gooding and Travis Fields. 3d printed strain gauge geometry and orientation for embedded sensing. In *58th AIAA/ASCE/AHS/ASC Structures, Structural Dynamics, and Materials Conference*. American Institute of Aeronautics and Astronautics, January 2017.
- [32] Kyuyoung Kim, Jaeho Park, Ji-hoon Suh, Minseong Kim, Yongrok Jeong, and Inkyu Park. 3D printing of multiaxial force sensors using carbon nanotube (CNT)/thermoplastic polyurethane (TPU) filaments. *Sensors and Actuators A: Physical*, 263:493–500, 2017.
- [33] Mohammed Al-Rubaiyai, Ryohei Tsuruta, Umesh Gandhi, Chuan Wang, and Xiaobo Tan. A 3d-printed stretchable strain sensor for wind sensing. *Smart Materials and Structures*, 28(8):084001, June 2019.
- [34] Michael Dawoud, Iman Taha, and Samy J Ebeid. Strain sensing behaviour of 3D printed carbon black filled ABS. *Journal of Manufacturing Processes*, 35:337–342, 2018.
- [35] Sithiprumnea Dul, Alessandro Pegoretti, and Luca Fambri. Fused filament fabrication of piezoresistive carbon nanotubes nanocomposites for strain monitoring. *Frontiers in Materials*, 7:12, 2020.
- [36] Wenli Ye, Wenzheng Wu, Xue Hu, Guoqiang Lin, Jinyu Guo, Han Qu, and Ji Zhao. 3d printing of carbon nanotubes reinforced thermoplastic polyimide composites with controllable mechanical and electrical performance. *Composites Science and Technology*, 182:107671, 2019.
- [37] Matic Arh, Janko Slavič, and Miha Boltežar. Experimental identification of the dynamic piezoresistivity of fused-filament-fabricated structures. *Additive Manufacturing*, 36:101493, December 2020.
- [38] Marco Maurizi, Janko Slavič, Filippo Cianetti, Marko Jerman, Joško Valentinčič, Andrej Lebar, and Miha Boltežar. Dynamic measurements using FDM 3d-printed embedded strain sensors. *Sensors*, 19(12):2661, June 2019.
- [39] Marco Maurizi, Filippo Cianetti, Janko Slavič, Guido Zucca, and Massimiliano Palmieri. Piezoresistive dynamic simulations of fdm 3d-printed embedded strain sensors: a new modal approach. *Procedia Structural Integrity*, 24:390 – 397, 2019. AIAS 2019 International Conference on Stress Analysis.
- [40] Kenneth McConnell. *Vibration testing : theory and practice*. John Wiley & Sons, Hoboken, New Jersey, 2008.

- [41] Branislav Notaros. *Electromagnetics*. Prentice Hall, Upper Saddle River, N.J, 2011.
- [42] Charles S Smith. Macroscopic Symmetry and Properties of Crystals. In Frederick Seitz and David B T Solid State Physics Turnbull, editors, *Advances in Research and Applications*, volume 6, pages 175–249. Academic Press, 1958.
- [43] Yingjun Zhao, Sandra Gschossmann, Martin Schagerl, Patrick Gruener, and Christoph Kralovec. Characterization of the spatial elastoresistivity of inkjet-printed carbon nanotube thin films. *Smart Materials and Structures*, 27(10):105009, September 2018.
- [44] J. N. Reddy. *An Introduction to Continuum Mechanics*. Cambridge University Press, July 2013.
- [45] Caterina Casavola, Alberto Cazzato, Vincenzo Moramarco, and Carmine Pappalettere. Orthotropic mechanical properties of fused deposition modelling parts described by classical laminate theory. *Materials & Design*, 90:453–458, January 2016.
- [46] Tianyun Yao, Juan Ye, Zichen Deng, Kai Zhang, Yongbin Ma, and Hua-jiang Ouyang. Tensile failure strength and separation angle of FDM 3D printing PLA material: Experimental and theoretical analyses. *Composites Part B: Engineering*, 188(November 2019):107894, 2020.
- [47] Yu Zhao, Yuansong Chen, and Yongjun Zhou. Novel mechanical models of tensile strength and elastic property of FDM AM PLA materials: Experimental and theoretical analyses. *Materials and Design*, 181:108089, 2019.
- [48] Singiresu S. Rao. *Vibration of Continuous Systems*. John Wiley & Sons, Inc., December 2006.
- [49] A. W. Leissa. Closed form exact solutions for the steady state vibrations of continuous systems subjected to distributed exciting forces. *Journal of Sound and Vibration*, 134(3):435–453, 1989.
- [50] Nuno Manuel Mendes Maia and Júlio Martins Montalvao e Silva. *Theoretical and experimental modal analysis*. Research Studies Press, 1997.
- [51] Klemen Zaletelj, Tomaž Bregar, Domen Gorjup, and Janko Slavič. ladisk/pyema: v0.24, September 2020.

- [52] Miquel Domingo-Espin, Josep M. Puigoriol-Forcada, Andres-Amador Garcia-Granada, Jordi Llumà, Salvador Borros, and Guillermo Reyes. Mechanical property characterization and simulation of fused deposition modeling polycarbonate parts. *Materials & Design*, 83:670–677, October 2015.
- [53] Dan Mihai Ștefănescu. *Handbook of Force Transducers*. Springer Berlin Heidelberg, 2011.
- [54] Technical data sheet - embossed tin-plated copper foil tape 1345 3m. <https://multimedia.3m.com/mws/media/373860/3m-embossed-tin-plated-copper-foil-tape-1345.pdf>. Last accessed 21. September 2020.
- [55] Technical data sheet - electrolube scp. [https://electrolube.com/knowledge\\_base/scp-technical-data-sheet/](https://electrolube.com/knowledge_base/scp-technical-data-sheet/). Last accessed 21. September 2020.
- [56] Pauli Virtanen, Ralf Gommers, Travis E. Oliphant, Matt Haberland, Tyler Reddy, David Cournapeau, Evgeni Burovski, Pearu Peterson, Warren Weckesser, Jonathan Bright, Stéfan J. van der Walt, Matthew Brett, Joshua Wilson, K. Jarrod Millman, Nikolay Mayorov, Andrew R. J. Nelson, Eric Jones, Robert Kern, Eric Larson, C J Carey, İlhan Polat, Yu Feng, Eric W. Moore, Jake VanderPlas, Denis Laxalde, Josef Perktold, Robert Cimrman, Ian Henriksen, E. A. Quintero, Charles R. Harris, Anne M. Archibald, Antônio H. Ribeiro, Fabian Pedregosa, and Paul van Mulbregt. SciPy 1.0: fundamental algorithms for scientific computing in python. *Nature Methods*, 17(3):261–272, February 2020.
- [57] W. E. Baker. Vibration frequencies for uniform beams with central masses. *Journal of Applied Mechanics*, 31(2):335–337, June 1964.